

Titanium Carbide MXene and Silver Nanowire Composite Ink for Transparent Flexible Printed Micro-Supercapacitors

Neha Sharma, Shravani Kale, Neethu Thomas, Sangeeta Kale, Debdutta Ray, and Parasuraman Swaminathan*

Micro-supercapacitors (*m*-SCs) are a competent power source for flexible and transparent electronics due to their compact and adaptive design. However, high-performance transparent *m*-SCs require an optimum balance between transparency and storage capacity. Herein, a composite of titanium carbide ($Ti_3C_2T_x$) and silver nanowires (Ag NWs) is proposed as electrodes for flexible and transparent *m*-SCs. This composite is synthesized in the form of a printable ink for direct ink writing (DIW) of the *m*-SC using poly(3,4-ethylenedioxythiophene):polystyrenesulfonate (PEDOT:PSS) as the conductive binder. The concentration of the Ag NWs, $Ti_3C_2T_x$, and PEDOT:PSS in the ink is optimized to ensure high

optical transparency, flexibility, and electrochemical performance of the *m*-SC. The optimized printed *m*-SC exhibits an areal capacitance of 8.34 mF cm^{-2} and a transparency of $\approx 82\%$ (at 550 nm) resulting in a high figure of merit of $15.1 \text{ F S}^{-1} \text{ cm}^{-2}$. It also shows high mechanical stability by retaining $\approx 97\%$ of its original capacitance in various bent positions. Printing of an *m*-SCs array is demonstrated in a single step by utilizing DIW. This array is used to power a surface-mount display LED. The obtained results for the developed *m*-SC promise its high suitability for futuristic, fully wearable, and invisible electronics.

1. Introduction

Flexible and transparent electronics are increasingly replacing conventional rigid electronics, driving innovations in displays, sensors, robotics, and communication.^[1–4] These electronics have inspired the development of complementary power sources with similar flexibility, along with high performance, light weight, and cost-effectiveness.^[5,6] Among existing power sources, micro-supercapacitors (*m*-SCs) provide flexibility over design and structure, while maintaining high electrochemical performance in terms of both power density and life stability.^[7–11] Hence, *m*-SCs are currently being developed as a flexible and lightweight power source for wearable electronic devices.^[12]

However, the challenge lies in making these *m*-SCs transparent.^[13] The typical inverse relationship between transparency and storage capacity raises the need to utilize electrochemically active materials that can provide high capacitance at minimal loading to maintain transparency.^[14]

MXenes, two-dimensional transition metal carbides/nitrides, are emerging pseudocapacitive materials with large specific surface area due to ingrained porosity and presence of electrochemically active sites for charge storage.^[15,16] MXenes-based *m*-SCs have been mostly fabricated using direct ink writing (DIW) technique, which is a type of 3D extrusion printing.^[17–20] The inks in DIW are loaded into syringes with adjustable nozzle diameters and are extruded through pressure. This pressure-based extrusion process provides freedom over the choice of active material and enables the printing of their inks over a wide range of viscosities.^[21,22] MXenes-based printable inks generally require a highly concentrated dispersion to obtain a continuous conductive network due to self-restacking and aggregation issues in MXenes flakes. Fagade et al. studied ink properties for varied concentrations of MXenes to produce free standing inkjet-printed architectures and reported a high concentration of 100 mg mL^{-1} as optimum for such applications.^[23] Orangi et al. employed super-absorbent polymer beads to concentrate MXenes dispersion to a high value of 290 mg mL^{-1} and used it as a conductive ink for 3D printing of *m*-SC structures.^[24] The fabricated *m*-SC demonstrated excellent electrochemical performance with a high areal capacitance of 1035 mF cm^{-2} but was not transparent. One strategy to minimize the required concentration of MXenes and achieve mechanically robust MXenes-based SC electrodes while maintaining high electrochemical performance is to form a composite of MXene with various polymers.^[25,26] Combining MXenes with polymers, especially conducting polymers such as poly(3,4-ethylenedioxythiophene):polystyrene sulfonate (PEDOT:PSS) and

N. Sharma, N. Thomas, P. Swaminathan
Electronic Materials and Thin Films Lab
Department of Metallurgical and Materials Engineering
Indian Institute of Technology Madras
Chennai 600036, India
E-mail: swamnthy@iitm.ac.in

N. Sharma, D. Ray
AMOLED Research Center
Department of Electrical Engineering
Indian Institute of Technology Madras
Chennai 600036, India

S. Kale, S. Kale
Department of Applied Physics
Defence Institute of Advanced Technology
Girinagar, Pune 411025, India

P. Swaminathan
Centre of Excellence in Ceramics Technologies for Futuristic Mobility
Indian Institute of Technology Madras
Chennai 600036, India

 Supporting information for this article is available on the WWW under <https://doi.org/10.1002/batt.202500319>

polyaniline (PANI), addresses self-restacking issues in MXenes providing intact conductive electrodes and adding mechanical flexibility to the *m*-SC.^[27] For instance, a freestanding flexible MXenes and PANI nanoparticles hybrid film was produced with a low mass loading of 5 mg cm⁻² to develop SC electrodes exhibiting a high capacitance of 1885 mF cm⁻².^[28] Moreover, utilizing PANI as a composite material provided a well interconnected conductive network enhancing the ion transportation and hence, electrochemical performance. Composite gel ink of MXene with PEDOT:PSS has also been reported for the direct ink writing of printed flexible *m*-SCs achieving a high areal capacitance of 889 mF cm⁻².^[29]

Although MXenes and its polymer composites have shown high electrochemical performance, developing transparent SC requires a thin layer of single MXene sheets for the light to pass through the electrodes.^[30–32] This restriction limits the storage capacity of MXenes-based SCs. The variation in the capacitance and transmittance with the thickness of the MXenes films has been extensively studied through various fabrication techniques. One of the examples is inkjet-printed MXene-based transparent SC electrode, in which the thickness of electrodes was varied with the concentration of MXenes in the ink. The capacitance obtained for this electrode at a transmittance of 87% was 187.5 μF cm⁻². The capacitance value could be increased up to 1225 μF cm⁻² but only at the expense of reducing the transparency to merely 24%.^[33] Another similar example is spin-coated MXenes films where the transmittance of the films was reduced by 51% to achieve a capacitance gain of only 2.92 mF cm⁻².^[34] There has been an effort to fabricate flexible and transparent film SC by using MXene and PEDOT:PSS composite electrode, however, it could only produce an areal capacitance of 3.1 mF cm⁻² at a transmittance of 61.6% (@550 nm), which is much lower than other flexible and transparent SCs.^[35] Hence, an additional material that can provide high transparency and conductivity is needed to maintain the high electrochemical performance of MXenes and avoid thin-layered MXenes to produce transparent electrodes.

Silver nanowire (Ag NW) films have been demonstrated as one of the most reliable flexible and transparent conducting films till now. Ag NWs are already deployed in the market as an integral component in various devices, such as displays.^[36,37] Ag NWs are often combined with MXenes to use them as transparent conducting films for electromagnetic interference shielding, electro-luminescent devices, and organic solar cells.^[38–40] Ag NWs are also reported as a synergistic companion for MXenes to facilitate the charge/ion transport in the SC electrodes due to its high electronic conductivity.^[41,42] However, the high transparency that can be achieved with a highly conductive percolation network of Ag NWs has not been taken advantage of to fabricate MXenes-based transparent *m*-SCs.

In this work, we utilized the highly electrochemically active Ti₃C₂T_x MXene and the conductive percolative network of Ag NWs to fabricate high performance, flexible, and transparent *m*-SC. This combination removes the necessity to produce ultrathin MXene films for transparent SC electrodes which lacks storage capacity. A composite ink of Ti₃C₂T_x and Ag NWs was formulated, along with PEDOT:PSS, for DIW of *m*-SC. The Ti₃C₂T_x in the electrode provided high capacitance, Ag NWs provided high

electrical and optical conductivity, and PEDOT:PSS provided chemical stability. This composite electrode resulted in an *m*-SC with a specific areal capacitance of 8.34 mF cm⁻² with a transparency of ≈82% at 550 nm and retained 81% of its original capacitance even after 10 000 galvanic charge-discharge cycles. Moreover, the *m*-SC showed high mechanical robustness by retaining ≈90% capacitance after 500 cycles of bending at 0.6 cm distance. Finally, an *m*-SCs array was printed in a single step with the use of DIW to demonstrate its applicability as a power source for a surface-mount display (SMD) LED.

2. Results and Discussion

2.1. Structural and Morphological Analysis of Ti₃C₂T_x-30 and Ag NWs

The X-ray diffraction (XRD) curve for titanium aluminum carbide (Ti₃AlC₂) MAX and Ti₃C₂T_x-30 MXene are depicted in Figure 1a. The XRD peaks observed in MAX were at 9.55°, 19.13°, 35.98°, 38.78°, 41.78°, and 60.55°. These peaks belong to the (0 0 2), (0 0 4), (1 0 3), (1 0 4), (1 0 5), and (1 1 0) planes, respectively.^[43] When this Ti₃AlC₂ MAX was exposed to hydrofluoric (HF) acid, the Al layer is etched out which can be observed by the absence of 20 peak at 38.78° in Ti₃C₂T_x-30 MXene. The peaks seen in Ti₃C₂T_x-30 MXene were prominently into the (0 0 1) plane orientation, as suggested by literature.^[44] The XRD pattern revealed the hexagonal structure of the synthesized MXene. Also, the corresponding XRD peaks for Ti₃C₂T_x-30 MXene were obtained at lower angles as compared to Ti₃AlC₂ MAX, suggesting increased d-spacing in MXene structure. For example, the 2θ value observed in Ti₃AlC₂ MAX structure for (0 0 2) plane was at 9.55° whereas in case of Ti₃C₂T_x-30 MXene it was at 9.07°.

Figure S2, Supporting Information and Figure 1b represent the field emission scanning electron microscopy (FE-SEM) images of Ti₃AlC₂ MAX phase and Ti₃C₂T_x-30 MXene, respectively. FE-SEM was utilized to investigate the morphology of MAX and synthesized MXene material. The FE-SEM pictures showed two-dimensional accordion-like sheets of Ti₃C₂T_x-30 MXene. These accordion-like structures represent multilayered sheets with a significantly enhanced surface area when compared to their parent MAX phases. The etching out process of Al layer with HF acid results in the evolution of H₂ gas which expands and delaminates the layers in Ti₃C₂T_x-30 MXene (Figure 1b). The morphology of Ti₃AlC₂ resembled a stacked block. This also implies that Ti₃C₂T_x-30 MXene has a higher surface area and electrochemically active sites than the Ti₃AlC₂ MAX structure. TEM images of Ti₃C₂T_x-30 MXene are depicted in Figure 1c. The two-dimensional flakes were clearly revealed after the probe sonication of the Ti₃C₂T_x-30 solution. The selected area electron diffraction pattern also confirmed the hexagonal structure of Ti₃C₂T_x-30 (Figure 1d), as predicted through XRD pattern. The smaller flakes of the MXene create more pathways facilitating ion transport and have large number of electrochemically active sites for charge storage.^[45] Larger flakes maintain high electronic conductivity in the electrodes due to lower flake-flake contact resistance.^[46] Hence, the solution obtained after ultrasonication was used without any

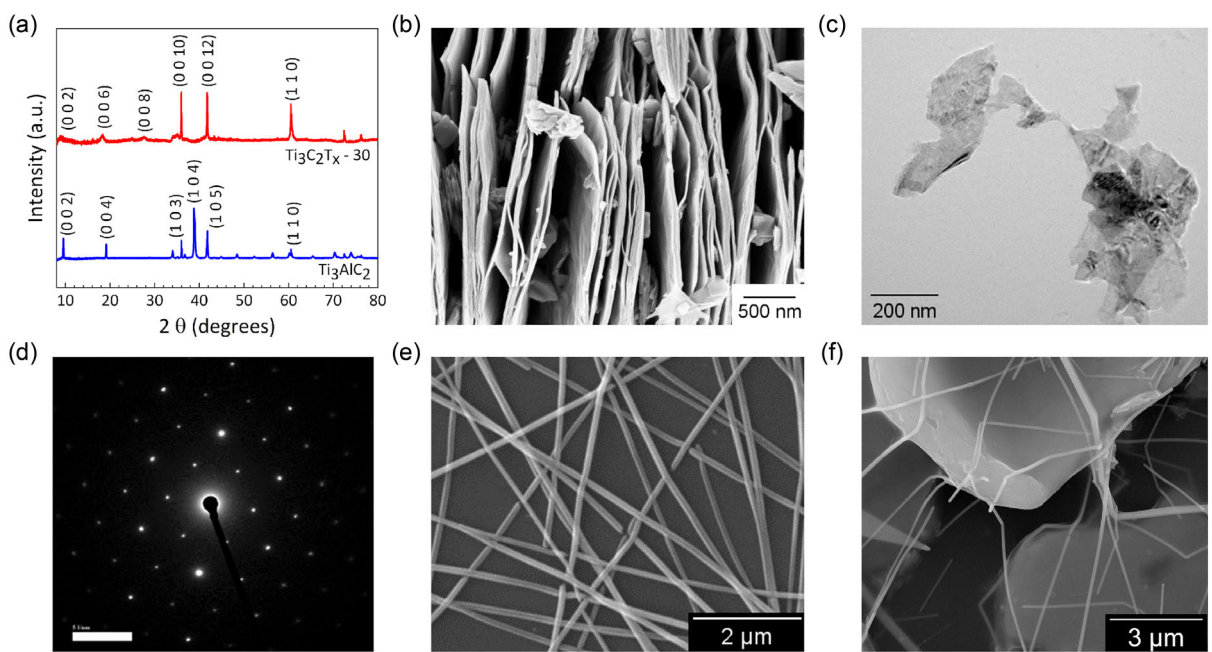


Figure 1. a) X-ray diffraction (XRD) pattern of Ti_3AlC_2 MAX and $\text{Ti}_3\text{C}_2\text{T}_x\text{-}30$ MXene. b) Scanning electron microscopy (SEM) images of $\text{Ti}_3\text{C}_2\text{T}_x\text{-}30$ showing the accordion-like morphology of $\text{Ti}_3\text{C}_2\text{T}_x\text{-}30$. c) and d) Transmission electron micrographs and selected area electron diffraction pattern of $\text{Ti}_3\text{C}_2\text{T}_x\text{-}30$ sheets, respectively. e) and f) SEM images of silver nanowires (Ag NWs) obtained from polyol synthesis and $\text{Ti}_3\text{C}_2\text{T}_x\text{-}30/\text{Ag NWs}/\text{PEDOT:PSS}$ composite, respectively.

filtration to formulate the composite inks, thus making use of both the smaller and larger flakes.

In the synthesis of Ag NWs, silver nitrate (AgNO_3) serves as the precursor for silver metal, while ethylene glycol (EG) acts as both the solvent and reducing agent (in the form of glycolaldehyde). Ferric chloride (FeCl_3) is used as a growth promoter. Ag ions are reduced by EG, which results in the formation of multiply twinned decahedral seed particles, which then continue to grow into nanowires.^[47] Polyvinylpyrrolidone (PVP) functions as a capping agent that effectively confines the {100} facets on the lateral surface of NWs in comparison to the {111} growing facets, thereby facilitating one-dimensional growth from these seed particles.^[47] The polycrystalline structure of the NWs was confirmed through XRD pattern (Figure S3a, Supporting Information). The morphology of Ag NWs obtained from polyol synthesis was observed in scanning electron microscopy (SEM) image (Figure 1e). The average length and diameter of the Ag NWs were measured to be $60.6 \pm 15.1 \mu\text{m}$ and $104.0 \pm 19.1 \text{ nm}$, respectively (Figure S3b,c, Supporting Information). The longer and wider Ag NWs provide a percolative network with high optical and electrical conductivity even at minimal loading, hence, are optimum for transparent conducting electrodes.^[47,48]

2.1. Electrochemical Analysis of the $\text{Ti}_3\text{C}_2\text{T}_x\text{-}30$ and Ag NWs Composite m-SC Electrodes

The combination of random sized $\text{Ti}_3\text{C}_2\text{T}_x\text{-}30$ flakes and long Ag NWs was utilized to fabricate the *m*-SC with high electrochemical performance along with high transparency and mechanical flexibility. This combination was also accompanied by the conducting polymer, PEDOT:PSS, to maintain the chemical stability of the

m-SC electrodes and provide a conductive bridge between the $\text{Ti}_3\text{C}_2\text{T}_x\text{-}30$ flakes and Ag NWs. The conductive percolative network formed in this composite is displayed in Figure 1f. This composite was used in the form of ink to print the *m*-SC electrodes using a custom-built direct ink writer which can print inks over a wide range of viscosities.^[49,50] Hence, the polymer gel electrolyte could also be printed using the same writer resulting in a fully printed *m*-SC.

The concentration of each material in the composite ink should be optimized to achieve high performance of the *m*-SC electrodes. Hence, the composite inks with different concentrations (0 to 1.5% w/v) of $\text{Ti}_3\text{C}_2\text{T}_x\text{-}30$ in a fixed Ag NWs and PEDOT:PSS solution (optimized in our prior work)^[49] were prepared and used to print the *m*-SC electrodes. A basic cyclic voltammetry (CV) test was conducted on the printed *m*-SCs, with different concentrations of $\text{Ti}_3\text{C}_2\text{T}_x\text{-}30$, to compare and analyze the charge storage performance and optical transparency. The CV curves were obtained at 10 mV s^{-1} between a voltage range of 0–1 V (Figure 2a). The area under the CV curves, which is directly related to the amount of stored charge, increased and the transparency of *m*-SC decreased with increasing concentration of $\text{Ti}_3\text{C}_2\text{T}_x\text{-}30$ as expected (Figure 2b). A five-fold increase in the capacitance and appearance of redox peaks were observed with 0.5 wt% of $\text{Ti}_3\text{C}_2\text{T}_x\text{-}30$ due to pseudocapacitive charge storage from the electrochemically active sites in the $\text{Ti}_3\text{C}_2\text{T}_x\text{-}30$ and increased electric double layer capacitance (EDLC) from the higher surface area of the electrode (Table S1, Supporting Information). The capacitance didn't increase proportionally with further increase in concentration as the added $\text{Ti}_3\text{C}_2\text{T}_x\text{-}30$ provides more active sites but also hinders available active sites at the same time (Table S1, Supporting Information). These changes can also be understood through the thickness and

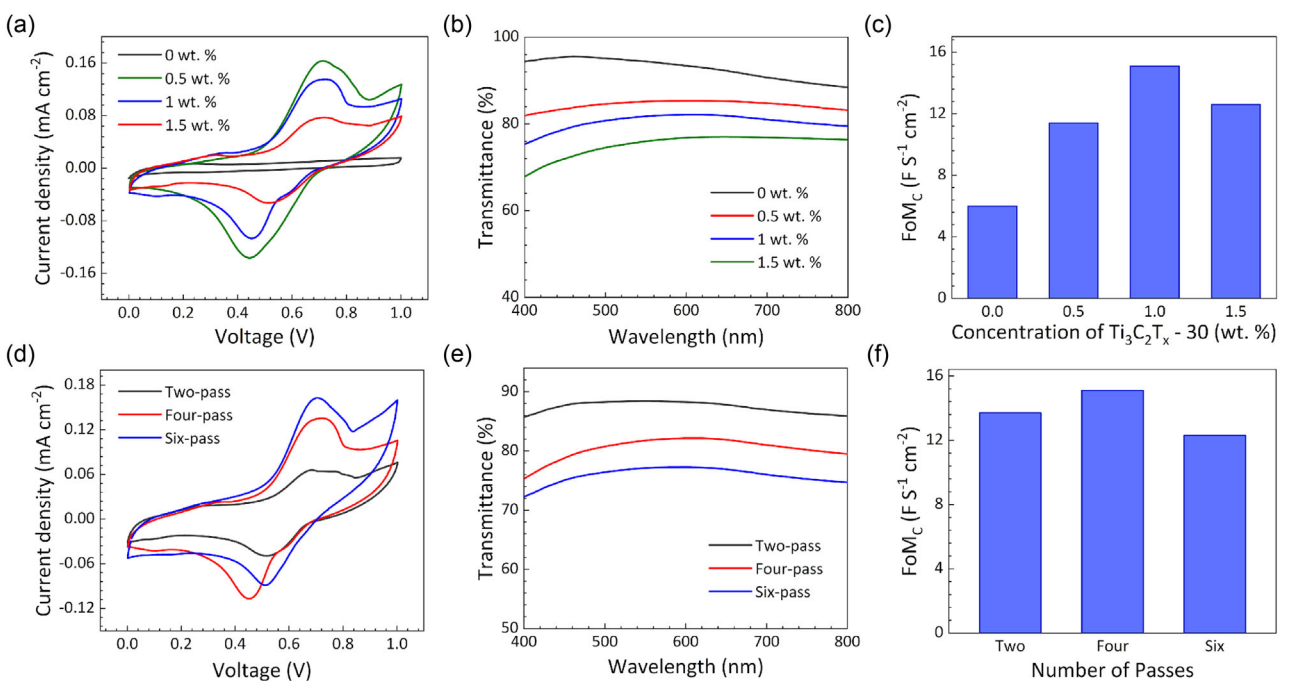


Figure 2. Comparative a) Cyclic voltammetry (CV) profiles, b) optical transmittance spectrum, and c) figure of merit (FoM_c) values obtained for the micro-supercapacitors (*m*-SCs) with increasing concentration of Ti₃C₂T_x-30. d) CV profiles, e) optical transmittance spectrum, and f) FoM_c values obtained for the increasing number of printing passes.

surface roughness data on the printed electrodes (Figure S4, Supporting Information). Higher concentrations of Ti₃C₂T_x-30 form 3D like islands which does provide more surface area but also hides the available Ti₃C₂T_x-30 (Figure S4, Supporting Information). These islands were only formed after adding Ti₃C₂T_x-30 and the surface roughness showed a large increase from 23.1 ± 3.1 nm (0% w/v) to 155.6 ± 2.2 nm (0.5% w/v) and hence, the capacitance. The increased surface roughness and thickness with increasing Ti₃C₂T_x-30 concentration are tabulated in Table S1, Supporting Information. Hence, to reach an optimized electrochemical performance and transparency, a figure of merit (FoM_c) was evaluated using formula S5 to qualify the electrochemical performance and transparency of the printed *m*-SCs. As seen in Figure 2c, the highest FoM was obtained for the electrodes with Ti₃C₂T_x-30 concentration of 1% w/v. After optimizing the concentration of Ti₃C₂T_x-30 to 1% w/v, the change in the electrochemical performance and transmittance was also studied by varying the number of printing passes from two to six (Figure 2d,e). There was an increase in the areal capacitance and a decrease in the transmittance as expected with increasing thickness of the electrodes (Table S2, Supporting Information). Another factor contributing to the enhanced capacitance in the *m*-SC is the increased electrode width and hence, decreased electrode spacing with printing passes (Figure S1 and Table S2, Supporting Information). In general, increasing the ratio of electrode width to electrode spacing enhances the performance of an *m*-SC.^[51] To find the optimized number of printing passes, FoM_c was again evaluated and four-pass printed electrodes produced the highest FoM_c (Figure 2f). Hence, the four-pass electrodes with 1% w/v of Ti₃C₂T_x-30 were considered for further electrochemical performance analysis.

The CV curve obtained in a voltage window of 0 to 1 V (safe operating voltage for aqueous electrolytes) for Ti₃C₂T_x-30 (1% w/v)/Ag NWs/PEDOT:PSS *m*-SC showed a couple of redox peaks separated by a small voltage (Figure 3a). The electrochemical phenomena contributing to the total charge stored in the *m*-SC include both faradic and non-faradaic processes. Faradaic processes arise due to the intercalation/deintercalation of H⁺ ions between the Ti₃C₂T_x-30 layers, which is a slow diffusion-controlled process, and the changes in the Ti oxidation state during the fast charge-transfer at the active electrode surface, which is known as pseudocapacitive process.^[52] On the contrary, non-faradaic processes are represented by the adsorption and desorption of ions at the electrode/electrolyte interface resulting in EDLC.^[53] The redox peaks in the CV curves show the dominance of pseudocapacitance due to the presence of Ti₃C₂T_x-30 as there were no redox peaks for pure Ag NWs and PEDOT:PSS electrode (Figure 2a).^[49] The area under the CV curve was used to evaluate the specific areal capacitance as 8.34 mF cm^{-2} (formula S1). The transmittance of this *m*-SC was 82% at 550 nm (Figure 3b). The specific areal capacitance and transmittance values resulted in a FoM_c of $15.1 \text{ F S}^{-1} \text{ cm}^{-2}$. The CV curves were also obtained at various scan rates ranging from 5 to 200 mV s^{-1} (Figure 3c). The peaks in the CV curves broadened with increasing scan rates showing the increase in EDLC at higher scan rates. Similar results were observed in the galvanostatic charge-discharge (GCD) curves displaying the distorted triangular curves at various current densities due to the pseudocapacitive nature of Ti₃C₂T_x-30 (Figure 3d). These distortions seemed to be decreasing with increasing current densities due to the domination of fast charge transfer and EDLC behavior for higher current density. The power and energy density of the *m*-SC was evaluated from the GCD curves as $1.5 \mu\text{W h cm}^{-2}$ and 0.6 mW cm^{-2} , respectively (formula S2–S4, Supporting Information). The comparison of

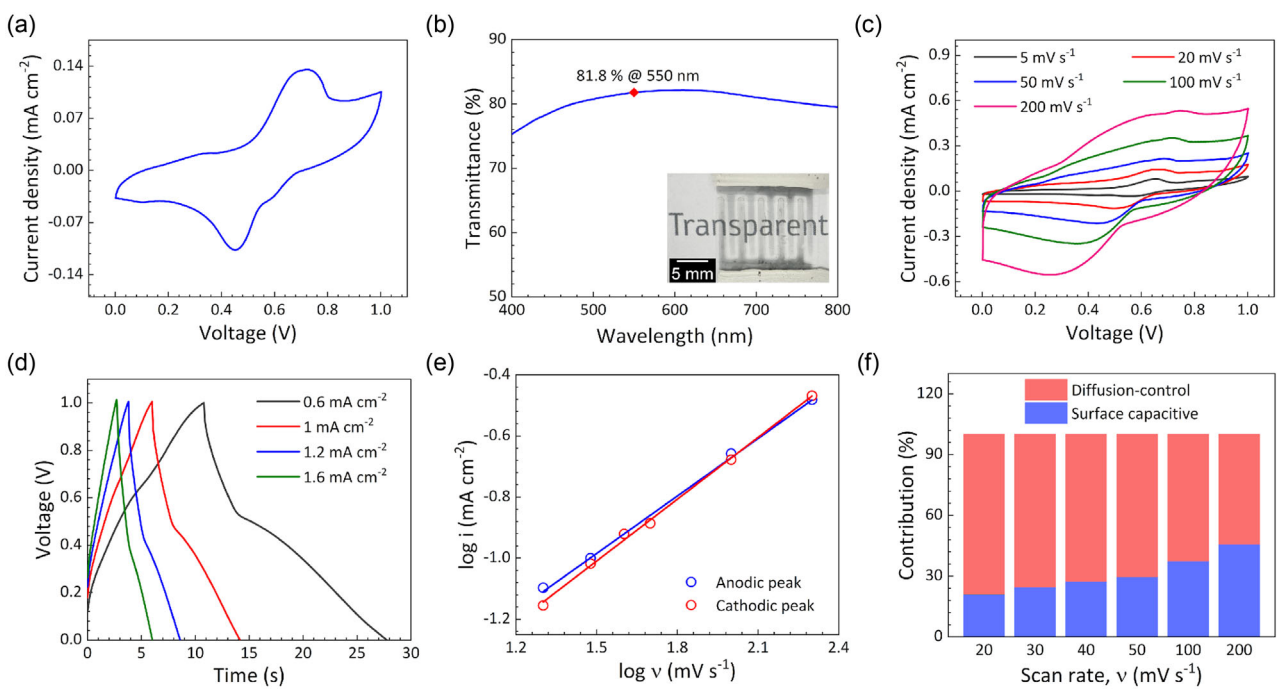


Figure 3. a) CV curve of the $\text{Ti}_3\text{C}_2\text{T}_x\text{-}30$ (1% w/v)/Ag NWs/PEDOT:PSS *m*-SC showing the generated redox peaks. b) Optical transmittance spectra of the printed *m*-SC device. (Inset: photograph of the *m*-SC showing its transparency). c,d) CV and galvanostatic charge-discharge (GCD) curves at varied scan rates and current densities, respectively. e) Logarithmic curve between the anodic/cathodic peak current and scan rate used to analyze charge storage processes. f) The charge storage contribution from diffusion-controlled and surface capacitive process at various scan rates.

these values with flexible and transparent SCs in literature was done using a Ragone plot (Figure S5, Supporting Information) and our results comparable to the reported *m*-SCs with highest energy and power density.

To further understand the involved charge storage mechanisms, the data of CV curves obtained at varied scan rates was analyzed using the equation given below,

$$i = av^b$$

where i is the current at anodic or cathodic peaks, v is the scan rate, and a and b are fitting parameters.^[54] The value of fitting parameter b defines the involved capacitive processes, where $b = 0.5$, that is, i being proportional to the square root of v , comes from diffusion-controlled faradic process of ion intercalation/deintercalation. Whereas $b = 1$ comes from surface capacitive process of EDLC and pseudo capacitance.^[51] For the $\text{Ti}_3\text{C}_2\text{T}_x\text{-}30$ (1% w/v)/Ag NWs/PEDOT:PSS *m*-SC, the b value was evaluated to be ≈ 0.7 , which indicates the involvement of both faradaic and non-faradaic processes (Figure 3e). The percentage of the diffusion-controlled and surface capacitive contributions was also evaluated using following equation from Dunn's method,

$$i(V) = k_1v + k_2v^{1/2}$$

where i is the total current at a particular voltage, v is the scan rate, and k_1 and k_2 are contribution constants.^[55] Here, $I \propto v$ is the current contribution from surface capacitive process and $I \propto v^{1/2}$ is the current contributed by diffusion-controlled process. The percentage contribution from both the phenomena is depicted in Figure 3f. It shows the percentage contribution from surface

capacitance changing from $\approx 21\%$ to $\approx 46\%$ indicating that the charge storage process is dominated by diffusion-controlled phenomenon at lower scan rates and moved toward surface capacitive at higher scan rates. These results confirms that the capacitance mainly comes from the intercalation pseudocapacitive behavior of $\text{Ti}_3\text{C}_2\text{T}_x\text{-}30$.

The cyclic stability of the printed *m*-SC was assessed by exposing the *m*-SC to 10 000 galvanic charge-discharges cycle at a current density of 1.2 mA cm^{-2} . Figure 4a shows the capacitance retained by the *m*-SC after various charge–discharge cycles. The increase in capacitance for the first 2000 cycles can be due to the deeper intercalation of ions into the $\text{Ti}_3\text{C}_2\text{T}_x\text{-}30$ layers that might be hidden in the islands formed of $\text{Ti}_3\text{C}_2\text{T}_x\text{-}30$ (Figure S4, Supporting Information).^[56] After this increase, the capacitance decreased and stabilized, retaining its original capacitance of 81%. This decrease can be attributed to the loss from the pseudo capacitance part of the charge storage as observed from the GCD curves at various cycles (Figure 4b). The electrolyte ion diffusion into the $\text{Ti}_3\text{C}_2\text{T}_x\text{-}30$ sheets might reduce with time due to evaporation of water from the gel electrolyte decreasing the overall electrochemical performance. Moreover, $\text{Ti}_3\text{C}_2\text{T}_x\text{-}30$ can undergo irreversible oxidation and interlayer delamination with increasing electrochemical cycles which affects its inherent properties such as electrical conductivity, structural integrity, specific surface area, and hence, the capacitance of $\text{Ti}_3\text{C}_2\text{T}_x\text{-}30$.^[41] Along with cyclic stability, the mechanical flexibility of the *m*-SC was also examined to show its viability as complementary power sources for flexible electronic devices. First the *m*-SC was exposed to various bending positions by varying the distance between the electrodes and it retained $\approx 96\%$ of its original capacitance at the

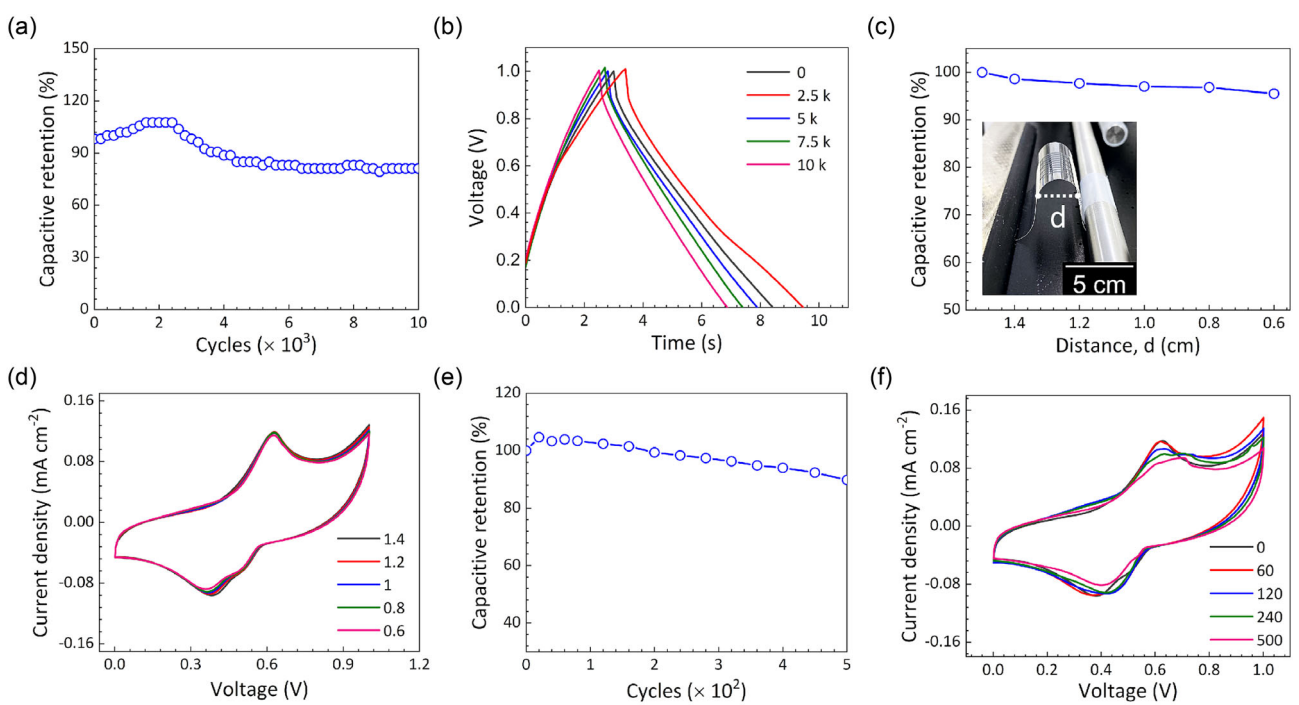


Figure 4. a) Capacitive retention curves for 10 000 GCD cycles. b) GCD curves for different GCD cycles obtained at a current density of 1.2 mA cm^{-2} . c) Capacitive retention and d) CV curves for varying bending distance between the electrodes, respectively. e) Capacitive retention and f) CV curves obtained over several bending cycles, respectively. A fraction of bending cycles is shown in video S1.

lowest bending distance of 0.6 cm (Figure 4c). Figure 4d shows the stable CV curves for the varied electrodes distance. The performance of *m*-SC was further tested for several bending cycles at bending distance of 0.6 cm and CV curves were obtained in-between the running bending cycles at 20 mV s^{-1} (Figure 4e,f). The *m*-SC was able to retain $\approx 90\%$ of its original capacitance after 500 bending cycles. These results from bending tests show the synergistic combination of $\text{Ti}_3\text{C}_2\text{T}_x$ -30 with Ag NWs and PEDOT:PSS, which maintain a conductive network between the $\text{Ti}_3\text{C}_2\text{T}_x$ -30 even in bent positions.

For the practical implementation of the $\text{Ti}_3\text{C}_2\text{T}_x$ -30 (1% w/v)/Ag NWs/PEDOT:PSS as a power source, it needs to be fabricated in the form of arrays. Hence, a 3×2 array was printed in a single step using the DIW technique followed by the printing of electrolyte. Figure 5a,b shows the CV and GCD curves for a single

m-SC and *m*-SCs array with the extended voltage (till 3 V) and increased discharge time. This array was further successfully tested as a power source for a SMD LED (Figure 5c).

The electrochemical, mechanical, and optical results obtained for the fabricated *m*-SC are compared with other flexible and transparent *m*-SCs reported in literature (Table 1). The FoM_c was evaluated for all the reported *m*-SCs and the *m*-SC fabricated in this work had comparatively higher FoM_c except the Ag NWs/Molybdenum disulfide (MoS_2) and Carbon nanotubes (CNTs)/Manganese dioxide (MnO_2) based *m*-SCs.^[57,58] However, these *m*-SCs were fabricated via multi-step, complicated, and time expensive procedures whereas our work produced fully printed *m*-SC using easy, fast, and scalable DIW technique in a single step. Moreover, this is the first report of a flexible and transparent MXenes-based *m*-SC in our knowledge. The successful

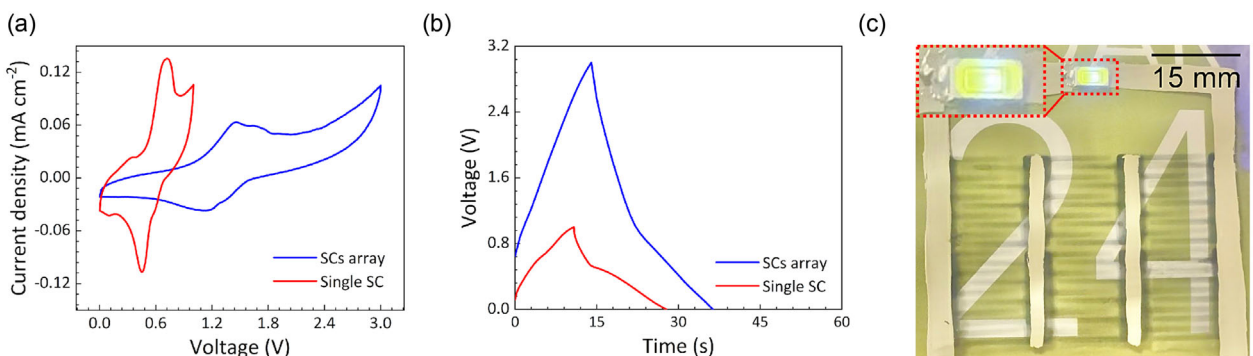


Figure 5. a) CV and b) GCD curves for single *m*-SC and array of *m*-SCs. c) Photograph of a printed *m*-SCs array showing it as a power source for SMD LED. The LED is also zoomed in the inset.

Table 1. Comparison of the optimized $\text{Ti}_3\text{C}_2\text{T}_x$ -30 (1% w/v)/Ag NWs/PEDOT:PSS *m*-SC in this work with flexible and transparent SCs from literature.

Ref.	Electrode	Fabrication	Transmittance [% @ 550 nm]	CA [mF cm ⁻²]	FoM _c ^a [F S ⁻¹ cm ⁻²]	Flexibility [retention%]
Our work	$\text{Ti}_3\text{C}_2\text{T}_x$ /Ag NWs/ PEDOT:PSS	DIW	82	8.34	15.1	$r_b = 6 \text{ mm}$ (97)
[49]	Ag NWs/PEDOT:PSS	DIW	84.6	3.68	7.8	$r_b = 5 \text{ mm}$ (93)
[57]	Ag NWs/MoS ₂	Spray coating/Laser writing	77.5	27.6	38.6	180° (98.6)
[59]	Graphene	Inkjet printing	87	0.012	0.3	$r_b = 2.75 \text{ cm}$ (93.1)
[60]	Polypyrrole	Etching	70.2	1.64	1.6	180° (90)
[58]	CNTs/ MnO ₂	Photolithography	79	12.6	18.8	30% stretching (96)
[61]	Ag NWs/PEDOT:PSS	EHD jet printing/spray coating	85	0.24	0.5	–
[62–69]	MnO ₂ /Au/Ni	Laser writing/electrodeposition/ nanoimprinting	81.7	1.33	2.4	$r_b = 7.5 \text{ mm}$ (95.5)

^aCalculated using formula S5.

optimization of the transparency, mechanical flexibility, and electrochemical performance of the fabricated $\text{Ti}_3\text{C}_2\text{T}_x$ -30 (1% w/v)/Ag NWs/PEDOT:PSS *m*-SC in this work proves its suitability as an integrated power source for flexible and transparent electronics.

3. Conclusion

In summary, a flexible and transparent $\text{Ti}_3\text{C}_2\text{T}_x$ -based *m*-SC was fabricated using DIW technique. High conductivity and transparency in the *m*-SC electrodes were achieved using Ag NWs and chemical stability was achieved using PEDOT:PSS. The concentration of $\text{Ti}_3\text{C}_2\text{T}_x$ and the number of printing passes were varied to optimized to obtain high electrochemical performance along with high transparency. The optimized *m*-SC electrodes had 1% w/v of $\text{Ti}_3\text{C}_2\text{T}_x$ and four passes of printing. This *m*-SC produced a specific areal capacitance of 8.34 mF cm^{-2} with a transparency of ≈82% at 550 nm. The mechanical stability of the *m*-SC was tested at various bending positions and bending cycles and it retained 90% of its original capacitance after 500 bending cycles at a bent electrode distance of 0.6 cm. The scalable advantage of DIW was utilized to print array of *m*-SCs which was displayed as a power source for SMD LED. These optimum electrochemical, transparency, and flexibility results promises the effective integration of this *m*-SC with next-generation flexible and transparent electronics.

4. Experimental Section

Synthesis of $\text{Ti}_3\text{C}_2\text{T}_x$ and Ag NWs

To synthesize $\text{Ti}_3\text{C}_2\text{T}_x$ MXene, a method from our prior work was adopted.^[40] In brief, 1 g of Ti_2AlC_2 MAX was etched in 30 wt% HF solution by stirring it at 300 rpm and at 30 °C for 30 h. The obtained solution was centrifuged and washed in deionized (DI) water at 7800 rpm for 10 min. This washing process was repeated till the supernatant's pH reached 7. Finally, the sediment from the centrifuged solution was freeze dried for 24 h and the dried powder, labeled $\text{Ti}_3\text{C}_2\text{T}_x$ -30, was stored in vacuum for further use.

Silver nanowires were synthesized using the polyol method, in which 0.163 g of PVP (Sigma-Aldrich, $M_w = 360\,000 \text{ g/mol}$) was dissolved in 22 mL of EG (99%, EMPARTA ACS). Following the full dissolution of PVP, 0.18 g of AgNO_3 (99%, Alfa Aesar) in 3 mL of EG and 2.5 mL of 0.6 mM FeCl_3 (97%, Sigma-Aldrich) in EG are added while stirring continuously. After five minutes, the mixture was transferred into a Teflon-lined stainless-steel autoclave and heated at 120 °C for 12 h. The reaction mixture was diluted with ethanol (premium grade, Heyman) in a 5:1 volume ratio once it had cooled. Ag NWs underwent three rounds of centrifugation at 1500 rpm for 15 min each, followed by an ethanol wash. The products were then dispersed in 2-Propanol (IPA, 99.5%, EMPARTA ACS) for storage purposes and characterization.

$\text{Ti}_3\text{C}_2\text{T}_x$ -30 and Ag NWs Composite Ink Formulation

The synthesized $\text{Ti}_3\text{C}_2\text{T}_x$ -30 powder was dispersed in N-methyl-2-pyrrolidone (NMP) at a concentration of 20% w/v. This dispersion was then ultrasonicated in a Branson CPX2800H bath sonicator for 5 h to reduce the flakes size of $\text{Ti}_3\text{C}_2\text{T}_x$ -30. To prepare the composite ink, $\text{Ti}_3\text{C}_2\text{T}_x$ -30 dispersion was first centrifuged at 10 000 rpm to remove NMP and redisperse in DI water. This $\text{Ti}_3\text{C}_2\text{T}_x$ -30 dispersion was mixed in PEDOT:PSS (PH1000, Sigma-Aldrich) and EG solution followed by 20 min of ultrasonication to prevent aggregation and self-restacking of $\text{Ti}_3\text{C}_2\text{T}_x$ -30. Finally, the $\text{Ti}_3\text{C}_2\text{T}_x$ -30:Ag NWs composite ink was obtained by adding 0.1% w/v of Ag NWs in the prepared $\text{Ti}_3\text{C}_2\text{T}_x$ -30 and PEDOT:PSS solution followed by 5 min vortex mixing. The concentration ratio between Ag NWs and PEDOT:PSS was kept the same, as optimized in our previous study to develop Ag NWs-based *m*-SC.^[41] Hence, in this work the $\text{Ti}_3\text{C}_2\text{T}_x$ -30 MXenes concentration was varied from 0 to 1.5% w/v, with a step of 0.5% w/v, to optimize the composition for a high performance flexible and transparent *m*-SC.

Fabrication of the Micro-Supercapacitor

A direct ink writer manufactured by Avay Biosciences Pvt. Ltd. was used to fabricate the *m*-SCs. The direct writer has two 1 mL syringe-based extruder setups, which can be used to print multiple inks. To print the *m*-SC, one of the extruders was loaded with the $\text{Ti}_3\text{C}_2\text{T}_x$ -30:Ag NWs composite ink and the other extruder with 1.18 M of H_3PO_4 (orthophosphoric acid)/PVA (polyvinyl alcohol) polymer gel electrolyte. This electrolyte was prepared by adding H_3PO_4 (85% purity, from Labchem) in 10% w/v PVA (solution, $M_w \approx 195\,000$, Merck) and mixed using a REMI 2MLH stirrer at 80 °C for 2 h. The interdigitated electrodes (IDEs) for *m*-SC were designed in Autodesk

Fusion software (dimensions displayed in Figure S1a, Supporting Information) and printed using a 24 G nozzle on a hydrophilic PET substrate kept at 50 °C bed temperature. The printing speed of 10 mm s⁻¹ and ink extrusion volume of 10 nL mm⁻¹ were fixed using the printer's D-write software. Consecutively, the gel electrolyte was printed over the IDEs also using a 16 G nozzle following by drying at 80 °C for 10 min. Finally, electrical connections were made using silver paste on the printed *m*-SC which was annealed at 80 °C for 20 min and used for electrochemical studies. An array of these *m*-SCs was also printed in a single step by designing this array in Autodesk Fusion software. This array was used to display its application as a power source.

Characterization

The structure of Ti₃C₂T_x-30 and Ag NWs was confirmed through XRD patterns obtained on a Bruker D8 advance X-ray diffractometer using Cu K_α radiation ($\lambda = 0.154$ nm). FE-SEM and SEM were performed on FEI NOVA NANOSEM 450 and Apreo S instruments respectively, for morphological analysis. Transmission electron microscopy images were captured on JEOL JEM F200 HRTEM at a resolution of 0.19 nm. ImageJ software was used to measure the nanowire dimensions. The optical characteristics and surface roughness of the printed *m*-SC electrodes were analyzed using JASCO V-660 UV-vis spectrophotometer and Bruker ContourGT optical profiler, respectively. Cyclic voltammetry and galvanic charge-discharge studies were performed using a Metrohm Autolab potentiostat/galvanostat 204, controlled by NOVA 2.1.6 software. A custom-built setup was made to obtain CV curves for the bent and unbent *m*-SC.

Acknowledgements

The work was supported by IIT Madras under the Institute of Eminence, India project number SB/2223/1272/MM/ETWO/008702. UV-Vis and SEM measurements were recorded at the Dept. of Metallurgical and Materials Engineering, IIT Madras. Centre for NEMS and Nanophotonics (CNMP) at Department of Electrical Engineering, IIT Madras helped with optical profilometry measurements.

Conflict of Interest

The authors declare no conflict of interest.

Author Contributions

Neha Sharma designed the experiment, fabricated the micro-SC, performed the electrochemical characterizations, and drafted the manuscript. **Shravani Kale** synthesized and characterized the titanium carbide MXene and performed its characterizations. **Neethu Thomas** synthesized and characterized silver nanowires. **Parasuraman Swaminathan, Debdutta Ray, and Shravani Kale** supervised and coordinated this study and revised the manuscript.

Data Availability Statement

The data that support the findings of this study are available from the corresponding author upon reasonable request.

Keywords: direct ink writing · flexible electronics · MXenes · silver nanowires · supercapacitors · transparent electrodes

- [1] K. Kim, Y.-G. Park, B. G. Hyun, M. Choi, J.-U. Park, *Adv. Mater.* **2019**, *31*, 1804690.
- [2] D. Won, J. Bang, S. H. Choi, K. R. Pyun, S. Jeong, Y. Lee, S. H. Ko, *Chem. Rev.* **2023**, *123*, 9982.
- [3] V. H. Nguyen, D. T. Papanastasiou, J. Resende, L. Bardet, T. Sannicolo, C. Jiménez, D. Muñoz-Rojas, N. D. Nguyen, D. Bellet, *Small* **2022**, *18*, 2106006.
- [4] D. Li, W.-Y. Lai, Y.-Z. Zhang, W. Huang, *Adv. Mater.* **2018**, *30*, 1704738.
- [5] H. Sheng, Y. Ma, H. Zhang, J. Yuan, F. Li, W. Li, E. Xie, W. Lan, *Adv. Mater. Technol.* **2024**, *9*, 2301796.
- [6] J. Liang, H. Sheng, H. Ma, P. Wang, Q. Wang, J. Yuan, X. Zhang, M. Shao, W. Li, E. Xie, W. Lan, *Adv. Mater. Technol.* **2023**, *8*, 2201234.
- [7] F. Bu, W. Zhou, Y. Xu, Y. Du, C. Guan, W. Huang, *Npj Flexible Electron.* **2020**, *4*, 31.
- [8] R. Jia, G. Shen, F. Qu, D. Chen, *Energy Storage Mater.* **2020**, *27*, 169.
- [9] J. Wang, F. Li, F. Zhu, O. G. Schmidt, *Small Methods* **2019**, *3*, 1800367.
- [10] H. Zhou, S. Gu, Y. Lu, G. Zhang, B. Li, F. Dou, S. Cao, Q. Li, Y. Sun, M. Shakouri, *Adv. Mater.* **2024**, *36*, 2401856.
- [11] W. Zong, Y. Ouyang, Y.-E. Miao, T. Liu, F. Lai, *Chem. Commun.* **2022**, *58*, 2075.
- [12] C. Zhao, Y. Liu, S. Beirne, J. Razal, J. Chen, *Adv. Mater. Technol.* **2018**, *3*, 1800028.
- [13] W. Zhao, M. Jiang, W. Wang, S. Liu, W. Huang, Q. Zhao, *Adv. Funct. Mater.* **2021**, *31*, 2009136.
- [14] F. Lin, P. Yang, Q. Wang, Y. Zhang, W. Wang, S. Liu, W. Zhao, Q. Zhao, *Adv. Mater. Technol.* **2023**, *8*, 2300972.
- [15] M. Hu, Z. Li, G. Li, T. Hu, C. Zhang, X. Wang, *Adv. Mater. Technol.* **2017**, *2*, 1700143.
- [16] S. Yong, C. Yao, N. Hillier, H. Kim, M. Holicky, S. Liu, R. Doherty, F. Torrisi, S. Beeby, *Adv. Mater. Technol.* **2024**, *9*, 2301266.
- [17] H. Huang, W. Yang, *ACS nano* **2024**, *18*, 4651.
- [18] N. Gupta, P. Saha, P. Bhattacharya, *Recent Progress Mater.* **2023**, *5*, 1.
- [19] E. Quain, T. S. Mathis, N. Kurra, K. Maleski, K. L. Van Aken, M. Alhabeb, H. N. Alshareef, Y. Gogotsi, *Adv. Mater. Technol.* **2019**, *4*, 1800256.
- [20] J. Ge, J. Meng, L. Zhang, J. Qin, G. Yang, Y. Wu, H. Zhu, Y. Huang, E. Debroye, H. Dong, others *Small* **2024**, *20*, 2312019.
- [21] M. Lay, M. G. Say, I. Engquist, *Adv. Mater. Technol.* **2023**, *8*, 2300652.
- [22] P. Yang, H. J. Fan, *Adv. Mater. Technol.* **2020**, *5*, 2000217.
- [23] M. Fagade, D. Patil, S. V. Thummalapalli, S. Jambhulkar, D. Ravichandran, A. M. Kannan, K. Song, *Mater. Adv.* **2023**, *4*, 4103.
- [24] J. Orangi, F. Hamade, V. A. Davis, M. Beidaghi, *ACS nano* **2019**, *14*, 640.
- [25] P. Forouzandeh, S. C. Pillai, *Curr. Opin. Chem. Eng.* **2021**, *33*, 100710.
- [26] S. A. Thomas, A. Patra, B. M. Al-Shehri, M. Selvaraj, A. Aravind, C. S. Rout, *J. Energy Storage* **2022**, *55*, 105765.
- [27] Q. Liu, J. Qiu, C. Yang, L. Zang, G. Zhang, E. Sakai, *Adv. Mater. Technol.* **2021**, *6*, 2000919.
- [28] X. Wang, Y. Wang, D. Liu, X. Li, H. Xiao, Y. Ma, M. Xu, G. Yuan, G. Chen, *ACS Appl. Mater. Interfaces* **2021**, *13*, 30633.
- [29] L. Li, J. Meng, X. Bao, Y. Huang, X.-P. Yan, H.-L. Qian, C. Zhang, T. Liu, *Adv. Energy Mater.* **2023**, *13*, 2203683.
- [30] T. Guo, D. Zhou, S. Deng, M. Jafarpour, J. Avaro, A. Neels, J. Heier, C. Zhang, *ACS nano* **2023**, *17*, 43737.
- [31] S. Kumar, D. Kang, V. H. Nguyen, N. Nasir, H. Hong, M. Kim, D. C. Nguyen, Y.-j. Lee, N. Lee, Y. Seo, *ACS Appl. Mater. Interfaces* **2021**, *13*, 40976.
- [32] J. Halim, M. R. Lukatskaya, K. M. Cook, J. Lu, C. R. Smith, L.-A. Naslund, S. J. May, L. Hultman, Y. Gogotsi, P. Eklund, M. W. Barsoum, *Chem. Mater.* **2014**, *26*, 2374.
- [33] D. Wen, X. Wang, L. Liu, C. Hu, C. Sun, Y. Wu, Y. Zhao, J. Zhang, X. Liu, G. Ying, *ACS Appl. Mater. Interfaces* **2021**, *13*, 17766.
- [34] C. Zhang, B. Anasori, A. Seral-Ascaso, S.-H. Park, N. McEvoy, A. Shmeliov, G. S. Duesberg, J. N. Coleman, Y. Gogotsi, V. Nicolosi, *Adv. Mater.* **2017**, *29*, 1702678.
- [35] S. Ren, X. Pan, Y. Zhang, J. Xu, Z. Liu, X. Zhang, X. Li, X. Gao, Y. Zhong, S. Chen, S. D. Wang, *Small* **2024**, *20*, 2401346.
- [36] Transparent conductive inks for flexible plastic layers — Genesink — genesink.com, <https://www.genesink.com/applications/transparent-conductive-film/>, [Accessed 12-12-2024].
- [37] D. Li, X. Liu, X. Chen, W.-Y. Lai, W. Huang, *Adv. Mater. Technol.* **2019**, *4*, 1900196.

- [38] N. Sharma, N. M. Nair, G. Nagasvari, D. Ray, P. Swaminathan, *Flexible Printed Electron.* **2022**, *7*, 014009.
- [39] H. Tang, H. Feng, H. Wang, X. Wan, J. Liang, Y. Chen, *ACS Appl. Mater. Interfaces* **2019**, *11*, 25330.
- [40] Y. Zhan, C. Santillo, Y. Meng, M. Lavorgna, *J. Mater. Chem. C* **2023**, *11*, 859.
- [41] H. Tang, R. Chen, Q. Huang, W. Ge, X. Zhang, Y. Yang, X. Wang, *EcoMat* **2022**, *4*, e12247.
- [42] L. Wang, Y. Tang, Y. Li, N. Wei, J. Yang, *Langmuir* **2022**, *38*, 7312.
- [43] S. Kale, S. Parmar, S. Datar, S. Kale, *Mater. Chem. Phys.* **2023**, *306*, 128052.
- [44] C. O. Ayiekpo, R. J. Musembi, A. A. Ogacho, B. O. Aduda, B. M. Muthoka, P. K. Jain, *Adv. Mater. Phys. Chem.* **2015**, *5*, 11458.
- [45] J. Tang, T. Mathis, X. Zhong, X. Xiao, H. Wang, M. Anayee, F. Pan, B. Xu, Y. Gogotsi, *Adv. Energy Mater.* **2021**, *11*, 2003025.
- [46] L. Jia, S. Zhou, A. Ahmed, Z. Yang, S. Liu, H. Wang, F. Li, M. Zhang, Y. Zhang, L. Sun, *Chem. Eng. J.* **2023**, *475*, 146361.
- [47] N. Thomas, N. Sharma, P. Swaminathan, *Nanotechnol.* **2023**, *35*, 055602.
- [48] M. Marus, A. Hubarevich, R. J. W. Lim, H. Huang, A. Smirnov, H. Wang, W. Fan, X. W. Sun, *Opt. Mater. Express* **2017**, *7*, 1105.
- [49] N. Sharma, A. M. Koshy, G. R. Kandregula, K. Ramanujam, D. Ray, P. Swaminathan, *ACS Appl. Energy Mater.* **2023**, *7*, 1363.
- [50] N. Sharma, G. R. Kandregula, A. M. Koshy, K. Ramanujam, D. Ray, P. Swaminathan, *Adv. Sustainable Syst.* **2024**, *9*, 2400649.
- [51] N. Liu, Y. Gao, *Small* **2017**, *13*, 1701989.
- [52] T. Jiang, Y. Wang, G. Z. Chen, *Small Methods* **2023**, *7*, 2201724.
- [53] J. Wang, J. Polleux, J. Lim, B. Dunn, *J. Phys. Chem. C* **2007**, *111*, 14925.
- [54] G. Zhou, M.-C. Li, C. Liu, Q. Wu, C. Mei, *Adv. Funct. Mater.* **2022**, *32*, 2109593.
- [55] X. Dong, Z. Guo, Y. Song, M. Hou, J. Wang, Y. Wang, Y. Xia, *Adv. Funct. Mater.* **2014**, *24*, 223405.
- [56] L. Li, N. Zhang, M. Zhang, X. Zhang, Z. Zhang, *Dalton Trans.* **2019**, *48*, 51747.
- [57] J. Li, Q. Shi, Y. Shao, C. Hou, Y. Li, Q. Zhang, H. Wang, *Energy Storage Mater.* **2019**, *16*, 212.
- [58] J. Yun, H. Lee, C. Song, Y. R. Jeong, J. W. Park, J. H. Lee, D. S. Kim, K. Keum, M. S. Kim, S. W. Jin, Y. H. Lee, *Chem. Eng. J.* **2020**, *387*, 124076.
- [59] S. S. Delekta, A. D. Smith, J. Li, M. Ostling, *Nanoscale* **2017**, *9*, 216998.
- [60] X. Jiao, C. Zhang, Z. Yuan, *ACS Appl. Mater. Interfaces* **2018**, *10*, 41299.
- [61] S.-W. Kim, K.-H. Lee, Y.-H. Lee, W.-J. Youe, J.-G. Gwon, S.-Y. Lee, *Adv. Sci.* **2022**, *9*, 2203720.
- [62] J.-P. Chen, W. Huang, Z.-Y. Jiang, J.-L. Xu, S.-Q. Zhao, Y.-H. Liu, *J. Phys. D: Appl. Phys.* **2020**, *53*, 165501.
- [63] N. A. Kyeremateng, T. Brousse, D. Pech, *Nat. Nanotechnol.* **2017**, *12*, 7.
- [64] L. Chen, P. Yao, W. Li, Q. Huang, J. Chen, H. Zhang, X. Wang, *ACS Appl. Mater. Interfaces* **2025**, *17*, 18666.
- [65] Z. Li, V. Ruiz, V. Mishukova, Q. Wan, H. Liu, H. Xue, Y. Gao, G. Cao, Y. Li, X. Zhuang, *Adv. Funct. Mater.* **2022**, *32*, 2108773.
- [66] S. B. Singh, T. Kshetri, T. I. Singh, N. H. Kim, J. H. Lee, *Chem. Eng. J.* **2019**, *359*, 197.
- [67] R. T. Ginting, M. M. Ovhal, J.-W. Kang, *Nano Energy* **2018**, *53*, 650.
- [68] B. S. Soram, J. Y. Dai, I. S. Thangjam, N. H. Kim, J. H. Lee, *J. Mater. Chem. A* **2020**, *8*, 24040.
- [69] H. Sheng, X. Zhang, Y. Ma, P. Wang, J. Zhou, Q. Su, W. Lan, E. Xie, C. J. Zhang, *ACS Appl. Mater. Interfaces* **2019**, *11*, 98992.

 Manuscript received: May 3, 2025

Revised manuscript received: July 3, 2025

Version of record online: